Proceedings World Geothermal Congress 2020+1
Reykjavik, Iceland, April - October 2021

Estimation of Permeability and Water Saturation from the Resistivity and Elastic Wave Velocity: Insight from Laboratory Experiment and Digital Fracture Simulation

Kazuki SAWAYAMA[1], Fei JIANG[2,3], Tatsunori IKEDA[3,4], Takuya ISHIBASHI[5], Takeshi TSUJI[3,4], Yasuhiro FUJIMITSU[4] and Hiroshi ASANUMA[5]

[1]Department of Earth Resources Engineering, Graduate school of Engineering, Kyushu University, 744 Motooka, Nishi-ku, Fukuoka, Fukuoka 819-0395, Japan
[2]Department of Mechanical Engineering, Graduate school of Sciences and Technology for Innovation, Yamaguchi University, 2-16-1 Tokiwadai, Ube, Yamaguchi 755-8611, Japan
[3]International Institute for Carbon-Neutral Energy Research, Kyushu University, 744 Motooka, Nishi-ku, Fukuoka, Fukuoka 819-0395, Japan
[4]Department of Earth Resources Engineering, Faculty of Engineering, Kyushu University, 744 Motooka, Nishi-ku, Fukuoka, Fukuoka 819-0395, Japan
[5]Fukushima Renewable Energy Institute, AIST, 2-2-9, Machiikedai, Koriyama, Fukushima 963-0298, Japan

k.sawayama0926@mine.kyushu-u.ac.jp

Keywords: fracture flow, elastic wave velocity, resistivity, Lattice Boltzmann Method, Enhanced Geothermal System

ABSTRACT

The estimation of fluid flow behavior (permeability and water saturation) in the fracture is essential for the sustainable development of geothermal resources. Recently, fluid flow in the geothermal reservoir has been attracting attention to succeed in EGS development. The fluid flow and its distribution under the ground could be detected by geophysical explorations (seismic and electromagnetic methods); however, the quantitative interpretation of these data is still difficult due to the lack of experimental data in fractured rocks. In this study, to discuss the effect of fluid flow behavior on these geophysical parameters, we measured and calculated them by using fractured rock samples that have different apertures and fluid distributions. For the numerical simulation, we firstly digitalize real rock fractures that are also used for laboratory experiments. The fluid flow simulations were then performed by using the Lattice Boltzmann Method. After analyzing the fluid distribution in the fracture, we conducted resistivity and elastic wave simulations by finite-element and finite-difference method, respectively. As a result of single-phase (water) flow analysis, permeability decreases with pressure increase in our experiment, and calculated permeability also shows the decrease as the aperture decreases. This agreement suggests that fracture permeability is constrained by aperture closure due to the pressure change. Our digital rock simulations reveal that changes in permeability and resistivity are controlled by disconnection of fluid connectivity, whereas velocity change is constrained by porosity variation due to fracture roughness. We also upscaled the relationship between fracture permeability, resistivity, and elastic wave velocity in a laboratory specimen to larger fracture dimensions and formulated their relationships regardless of the fracture sizes. Our empirical formula directly predicts changes in fracture permeability from geophysical properties, which may make it possible to monitor subsurface hydraulic activities through geophysical observations. In terms of the effect of fluid distributions under two-phase (water/gas) flow analysis, elastic wave velocity changed with the heterogeneity of fluid distribution while resistivity increases with higher connectivity of water even at the same water saturation and aperture conditions. Thus, elastic wave velocity or resistivity analysis has a difficulty to estimate the water saturation due to the complexity of fluid distribution. However, in contrast to this, our results suggest that the heterogeneity of fluid distribution can be expressed by aperture and connectivity from our digital rock fracture approach. Our results shed light on the potential of estimating fluid distribution by integrating seismic and electromagnetic explorations.

1. INTRODUCTION

Estimating fluid flow behavior in fractured rocks is crucial to develop geothermal resources not only for monitoring the reservoir condition (recovering or depleting), but also for developing Enhanced Geothermal Systems (EGS). In previous EGS (including Hot Dry Rock) projects, one of the biggest challenges was to control (or monitor) the injected water. Diffusion of the injected water caused a lower recovery rate (Kaieda, 2015) and was sometimes linked to induced seismicity (Majer et al., 2007). For fluid injection monitorings in EGS fields, resistivity changes associated with hydraulic stimulations were detected by means of Magnetotellurics (Peacock et al., 2012; 2013; Didana et al., 2017). In contrast, in the case of a non-stimulation type of EGS, few resistivity changes near the reservoir were so far monitored by means of Audio Magnetotellurics (Yamaya et al., 2018) during the artificial recharge into the depleted reservoir in Tohoku region, Japan. In addition to these resistivity monitoring cases, Taira et al. (2018) recently observed a long-term velocity increase, which may be related to the crack closure due to geothermal fluid production. Although these geophysical monitorings could detect the changes of reservoir condition, quantitative interpretations about the injected water distribution, permeability enhancement associated with aperture changes of fracture, and water saturation changes have not been evaluated yet. To monitor these fluid flow behavior from the geophysical observations, we should investigate the basic relationship between the hydraulic properties (permeability and water saturation) and geophysical properties (resistivity and elastic wave velocity) of rock.

Systematic changes in permeability, resistivity, and velocity have been studied based on crack propagation of intact rock (e,g., Paterson and Wong, 2004). Although some studies investigated the relationship of permeability-resistivity (Kirkby et al., 2016) of the fracture, there is no study investigating all rock properties simultaneously by using a real rock fracture with changing aperture. Since fracture geometry is unique, we have to investigate them simultaneously by using the same rock sample to see systematic changes. In this study, we investigated these properties by coupling approach of experiment and digital fracture simulation. Even

though the digital rock simulation approach has been broadly applied to various kinds of porous rock and has achieved success in relating elastic and hydraulic properties of rocks (e.g., Andrä et al., 2013; Yamabe et al., 2016; Tsuji et al., 2019), its application to the natural rock fracture has not been done. One of the most remarkable abilities of digital rock simulation is that we can evaluate the heterogeneous fluid flow evolution within the fracture that is difficult to visualize in a laboratory experiment.

Effect of water saturation on electric properties of rocks have been well investigated in porous rock (e.g., Archie, 1942; Knight, 1991; Su et al., 2000; Schmutz et al., 2012; Revil, 2013), and it is empirically known that resistivity is a function of the fluid resistivity, porosity, and water saturation. This empirical relationship (i.e., Archie's law) has been broadly applied to the interpretation of oil fields and CCS (Carbon Capture and Storage) test fields; however, the problem is that this equation is an empirical law based on experimental observations of porous rocks (e.g., sandstone). Since some studies reported that the resistivity-saturation relationship is not unique in the fractured sample (Sandler et al., 2009; Sawayama et al., 2018a), the applicability of Archie's law to the fracture should be discussed further, including numerical studies. As for the saturation effect on elastic properties of rocks, an increase in elastic wave velocity is confirmed experimentally as water saturation increases (e.g., Murphy, 1982; Endress and Knight, 1991). However, these studies also used porous rocks as samples. To the best of our knowledge, there is no study observing the saturation effect on the velocity change for the real rock fractures. The present study conducted simultaneous monitoring of velocity and resistivity of the real rock fracture in both experiment and numerical simulation. Since some studies in porous rocks reported that velocity and resistivity show different trends as a function of the saturation change (e.g., Nakatsuka et al., 2010), we discuss these trends in rock fractures.

In this study, we conducted simultaneous monitoring of resistivity and elastic wave velocity in both single-phase and two-phase fluid conditions by using single fractures. In single-phase fluid conditions, we investigated simultaneous changes in these rock properties with aperture closure in both natural fractures and upscaled synthetic fractures. Consequently, we established empirical models to estimate permeability by using resistivity and P-wave velocity that can link characteristics of small-scale and large-scale fractures. In two-phase fluid conditions, we evaluated the effect of water saturation on velocity and resistivity at various aperture conditions and discussed the importance of the effect of fluid distribution on them. Although resistivity decreases with increasing temperature, it is mainly due to the decrease of pore-fluid resistivity (e.g., Sen and Goode, 1992); that is to say, resistivity at higher temperature conditions can be estimated by simply assuming the pore-fluid resistivity at a certain temperature. The effect of temperature on P-wave velocity is not so significant at a temperature below 300 °C (Kern, 1978). Therefore, we here only changed the water saturation to simply determine the effect of water saturation on geophysical properties. We investigated these two problems (single-phase and two-phase) by coupling experiment and numerical approaches and interpreted how these geophysical properties change with the evolution of fluid flow properties.

2. METHOD

2.1 Sample preparation and digitalization

The fluid flow experiments and numerical simulations were carried out using cylindrical fractured samples of granite and andesite. The granite (Inada granite) consisted of medium-grain quartz, plagioclase, feldspar, and biotite (Sasada, 1991). The sample size of granite is 50 mm in diameter and 80 mm long, and contains a tensile fracture induced by a wedge. The andesite sample (35 mm in diameter and 70 mm long) from a fractured core retrieved at a geothermal area contains fine-grain quartz, plagioclase, calcite, and chlorite (Sawayama et al., 2018b). Fracture roughness of them was obtained by One-shot 3D Measuring Macroscope (KEYENCE, VR-3050). Roughness parameters and fractal dimension (estimated by a spectral method; Power et al., 1987; Power and Durham, 1997) of the footwall and hanging wall are summarized in Table 1.

Table 1. Fractal dimension and roughness parameters of granite and andesite

	Fractal dimension		Root mean square height (μm)	
	Footwall	Hanging wall	Footwall	Hanging wall
IG-1 (Granite)*	2.50	2.50	1290.7	1302.0
IG-2 (Granite)*	2.43	2.43	1688.9	1701.5
GA-1 (Andesite)**	2.45	2.46	540.43	535.65

*Data from Sawayama et al. (2020a).
**Data from Sawayama et al. (2020b).

From the obtained fracture roughness distribution of the footwall and hanging wall in each sample, we prepared three-dimensional digital fracture models by numerically pairing them (Fig. 1(A)). The aperture of the digital fracture (a gap between the footwall and hanging wall) was determined by a permeability matching approach in each pressure condition (e.g., Watanabe et al., 2008; Ishibashi et al., 2015). In addition to the natural fracture models, we also prepared upscaled synthetic fractures based on Matsuki et al. (2006) from the natural rough surfaces of andesite to verify the scale dependencies of rock properties (Sawayama et al., 2020b). The grid size of all digital models is 0.1 mm cubic.

2.2 Experimental procedure

Single-phase fluid flow experiments were performed under confining pressure ranging between 5 and 30 MPa and pore pressure ranging between 2 and 20 MPa. During the test, flow rate (Q) was monitored by a digital logger, and thereby permeability (k) could be calculated by the following equation (Darcy's law),

$$\frac{Q}{A} = \frac{k}{\mu}\frac{dp}{dx},$$

where A, μ, and dp/dx is a cross-sectional area, viscosity, and pressure gradient, respectively. Consequently, based on this equation, we estimated fracture permeability (k_f) as follows (e.g., Witherspoon et al., 1980);

$$k_f = \frac{e^2}{12},$$

where hydraulic aperture (e) is written by

$$e^3 = \frac{12\mu Q}{D}\frac{dx}{dp},$$

while D is the width of the fracture.

In addition to single-phase fluid flow experiments, we conducted two types of two-phase fluid flow experiments (imbibition test and drainage test) under 20 MPa of confining pressure (Sawayama et al., 2019). In imbibition tests, brine (1 wt.%-KCl) was injected into the sample at constant injection pressure at gas (nitrogen) saturated conditions to mimic the water injection into a depleted reservoir (filled with dry gas). After the imbibition tests, we carried out drainage tests: gas injection into the sample, which is saturated by brine initially. Since the drainage fluid was a two-phase mixture of brine and gas in our experiments, it was separated by a separator, and each volume of brine and nitrogen was measured by means of an electronic weighing instrument and a syringe pump, respectively. From these volumes and the injected brine volume, we can calculate the brine volume inside the sample, and thereby estimate the water saturation in the sample.

During each experiment, resistivity and elastic wave velocity were measured simultaneously. Resistivity was measured by a four-electrodes method under AC 30 mV of applied voltage (parallel to the flow direction). Elastic wave velocity was measured by a pulse transmission method (perpendicular to the flow direction). The input trigger of a pulse was set to 250 kHz of frequency and 10 Vp-p of amplitude.

2.3 Digital fracture simulation

From the digitally created fracture model, three-dimensional fracture flow was simulated by Lattice Boltzmann Method (e.g., He and Luo, 1997; Jiang et al., 2014). In Lattice Boltzmann Method (LBM), the fluid is replaced by a group of particles, and local fluid flow can be simulated as streaming and collision of these particles. The governing equation for LBM in the D3Q19 model is given by (Ahrenholz et al. 2008)

$$f_i(\boldsymbol{x} + e_i\,\Delta t,\, t + \Delta t) = f_i(\boldsymbol{x},\, t) + \boldsymbol{\Omega_i},\quad i = 0,\ \cdots 18,$$

where Δt is the time step and $f_i(\boldsymbol{x},\, t)$ is the particle distribution function that represents the probability of finding a particle at node $\boldsymbol{x}$ and time t with velocity $\boldsymbol{e}_i$. Collision operators $\boldsymbol{\Omega}$ are defined based on equilibrium moments and relaxation rates (Jiang et al., 2014). LBM has a remarkable ability to simulate heterogeneous local flow with complex boundaries (e.g., interactions between fluid-structure/fluid-fluid and heterogeneous fracture boundary). At the fracture surfaces, bounce-back boundaries (a no-slip scheme at fluid-solid interfaces) were implemented. Provision of a constant body force from the inlet to the outlet boundaries and the periodic boundary along the fracture plane enabled us to simulate the fracture flow (Fig. 1 (A)). Permeability along the fracture was estimated from the macroscopic flow velocity that was calculated from the particle distribution function (f_i).

From the heterogeneous water distribution estimated through the LBM simulation, resistivity and elastic wave velocity are calculated based on the finite-element method (Garboczi, 1998; Saxena and Mavko, 2016). Resistivity is estimated by obtained electric current associated with 30 mV of applied voltage in parallel to the flow direction. The electrical conductivity of Inada granite and geothermal andesite is taken to be 10^{-5} and 10^{-4} S/m, respectively, based on experimental results under dry conditions. Water and gas are modeled with 1.75 S/m and 10^{-14} S/m of conductivity, respectively, based on the experimental condition. Elastic wave velocity in the direction perpendicular to the fracture plane was estimated from the simulated static elasticity under the triaxial stress state. The elastic properties of solids for numerical simulation are determined based on velocity measurement of rocks under high-pressure condition; bulk modulus of solids in Inada granite and geothermal andesite is 58.6 GPa and 59.5 GPa, and shear modulus of solids in Inada granite and geothermal andesite is 31.0 GPa and 30.5 GPa, respectively. Water and gas are modeled with 2.25 GPa and 0.08 GPa of bulk modulus, respectively. The shear modulus of both fluids is modeled as 0 GPa. Since finite-element modeling predicts static elasticity, the result must be close to the solution based on Gassmann-Wood formula, which is a lower-frequency bound of elastic properties (Johnson, 2001). However, Makarynska et al. (2008) found that the results at the two-phase fluid condition from this method differ from Gassmann-Wood formula because the finite-element modeling failed to equilibrate fluid pressure throughout the pore space. Therefore, the velocity at the two-phase fluid condition in this study was estimated from three-dimensional dynamic wave simulations by using rotated staggered grid finite-difference method with second-order spatial and temporal operators (Saenger et al., 2000; Eng et al., 2017). This method is useful for the numerical model, which contains inhomogeneous structures such as crack or fracture (Bohlen and Saenger, 2006). 250 kHz of Ricker wavelet is used as a source function, and this plane source (vertical vibration) is added in a direction perpendicular to the fracture plane from the top of the model (Fig.1 (B)). The boundary condition of the z grid is a free surface. The x and y boundaries are periodic. We recorded the average particle velocity in each horizontal (xy) plane until 15,000 time steps (time interval is 0.1 ns). Figure 1 (C) represents an example of wave propagation through the digital fracture (AG-1) at 1.0 μs of elapsed time. From the first peak of waveforms at the top and bottom of the model, we calculated travel time and thereby estimated the velocity of each model.

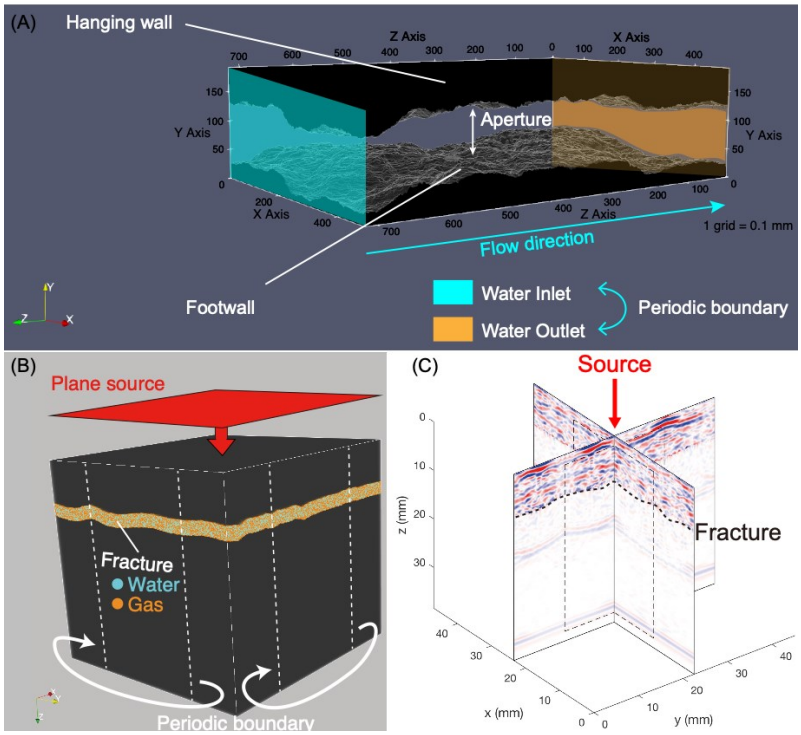

Figure 1: Model set-up and an example result of the digital fracture simulation. (A)Three-dimensional digitalized fracture of IG-1 and model set-up of Lattice Boltzmann fluid flow simulation, (B)a digital fracture model of GA-1 and model set-up of dynamic wave propagation simulation, and (C)an example of the snapshot of dynamic wave propagation at 1 μs of elapsed time. The color indicates the amplitude of the elastic wave (red and blue color take positive and negative value, respectively). Note that the grid size of each simulation is 0.1 mm in all directions.

3. RESULTS AND DISCUSSIONS

3.1 Single-phase fluid flow

Figure 2 shows three-dimensional water flows along the fracture plane in various aperture models. Water flow in each model forms preferential flow paths, which may reflect the local connectivity within a fracture. These flow paths decrease with aperture closure as well as a fluid flow area. Flow paths in Fig.2 (A), (B), and (C) are connected, while that in Fig.2 (D) is disconnected. As a result of permeability matching, Fig. 2 (A), (B), (C), (D) is corresponding to 0.7, 2.1, 4.1, 8.5 MPa of effective confining pressure, respectively.

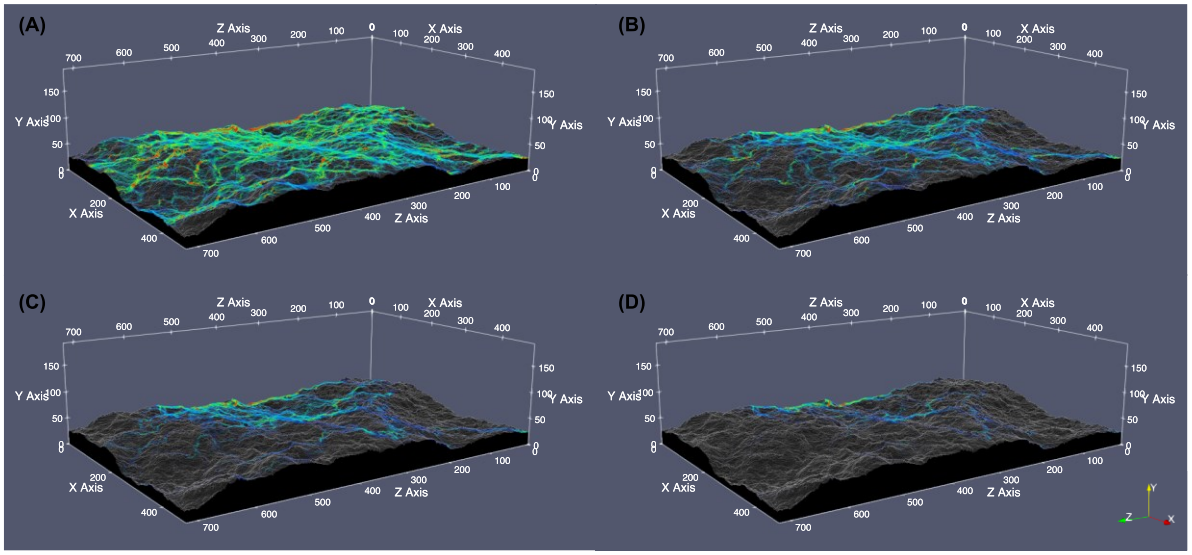

Figure 2: Three-dimensional fluid flow on the footwall of IG-1 fracture at (A) 0.18 mm, (B) 0.14 mm, (C) 0.12 mm, and (D) 0.10 mm of mean aperture condition. The color indicates the magnitude of flow velocity (red: high, blue: low), which is normalized by the maximum value of flow velocity at the condition of (A)—modified after Sawayama et al. (2020a).

As a function of estimated pressure, simultaneous changes in permeability, resistivity, P-wave velocity, and porosity are estimated (Fig. 3). Here, resistivity is plotted as the formation factor (F), which is the resistivity (ρ) normalized by fluid resistivity (ρ_f) as follows.

$$F = \frac{\rho}{\rho_f}$$

As a result, permeability and resistivity show a similar trend with increasing pressure, whereas the trend of velocity change with pressure is different. Permeability and resistivity are generally sensitive to the connectivity of fluid. The flow path in IG-1 fracture is disconnected at 8.5 MPa of pressure (Fig. 2 (D)) and that in IG-2 fracture is disconnected at 9.5 MPa of pressure. Both IG-1 and IG-2 fractures show inflection at these pressure conditions (percolation threshold), suggesting that permeability and resistivity trends with aperture closure could be explained by the connection or disconnection of flow paths. Elastic wave velocity varies notably with roughness, which arises from roughness dependency of porosity (Fig. 3) as well as spatial distributions of contacting asperities (Sawayama et al., 2020a).

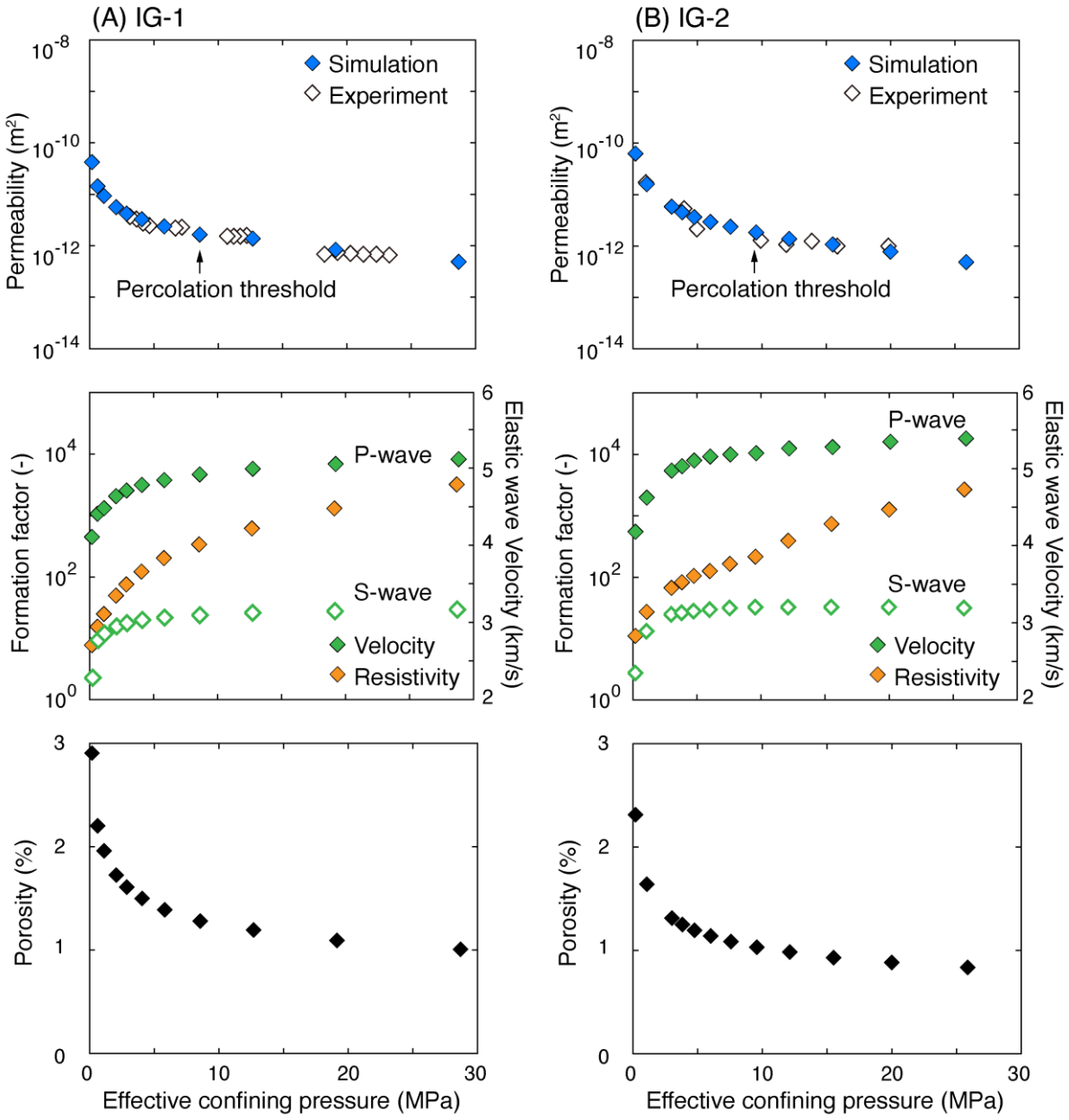

Figure 3: Simultaneous changes of permeability, resistivity, elastic wave velocity, and porosity against effective confining pressure. (A)Experimental result and simulation result of permeability, formation factor, P-wave velocity, and porosity in IG-1 fracture, (B) experimental result and simulation result of permeability, resistivity, elastic wave velocity, and porosity in IG-2 fracture. Note that resistivity is plotted as the formation factor that is the resistivity normalized by fluid resistivity—data from Sawayama et al. (2020a).

3.2 Empirical relationships between permeability and geophysical properties

Having explored the changes in permeability, formation factor, and P-wave velocity, we then examined the respective correlations under various ranges of fracture sizes using synthetic fractures (Fig. 4). Figure 4 (A) plots the relationship between permeability and P-wave velocity (*k–Vp* relationship hereafter). The *k–Vp* relationship is less sensitive to the fracture size in our models, and thus can be formulated as

$$\log(k) = \frac{aVp/Vp' - a}{-bVp/Vp' + b},$$

where Vp' is the reference P-wave velocity (in our case, 6.14 km/s), and a and b are empirical parameters that take 3.01×10^5 and 3.54×10^3 in the present study. Note that S-wave velocity can be modeled in a similar manner (Sawayama et al., 2020b). Since P-wave velocity depends on the roughness, according to Fig. 3, these parameters will be influenced by the initial surface roughness of the fracture. Overall, the *k–Vp* relationship may be less sensitive to the fracture size while the fracture has similar surface fractal characteristics (e.g., similar geological formation).

The relationship between fracture permeability and formation factor (*k–F* relationship hereafter) plotted in Fig. 4 (B) is also less sensitive to the fracture sizes. The *k–F* relationship can be empirically formulated as

$$\log k = -\alpha \cdot \log F - \beta,$$

where α and β are empirical parameters depending on ranges of permeability, for example, $\alpha = 1.0$ and $\beta = 8.0$ when $k < 10^{-10.8}$ m^2, whereas $\alpha = 1.8$ and $\beta = 5.7$ when $k > 10^{-10.8}$ m^2. The empirical parameter β is influenced by the number of fractures in a unit volume (i.e., fracture density), whereas the slope α remains constant regardless of the fracture density (Sawayama et al., 2020b). The offset β can be neglected for monitoring purposes as

$$\frac{k}{k'} = \frac{F^{-\alpha}}{F'}$$

where k' and F' are arbitrary reference values of the permeability and formation factor, respectively. Overall, the slope α remains constant regardless of the fracture size and roughness, as both permeability and formation factor are less sensitive to the roughness (Fig. 3). In practice, resistivity observations in Australian EGS projects have detected changes in resistivity of around 5% (Didana et al., 2017) and 10% (Peacock et al., 2013) associated with hydraulic stimulation of pre-existing fault systems. Assuming $\alpha = -1.8$, these resistivity changes correspond to 11% and 21% increases in permeability, respectively. Although α is potentially different in rock fracture surfaces with different fractal characteristics, it will take values between 1 and 2 (Sawayama et al., 2020b); indeed, permeability changes are always larger than observed resistivity changes. However, because our model assumes a simple vertical series of single fractures, the changes in transport properties in intersecting fracture networks (e.g., Kirkby and Heinson, 2017) should be further investigated. Moreover, it should be noted that permeability enhancement by hydraulic stimulation is triggered not only by joint openings but also by shear slips (e.g., Rinaldi and Rutqvist, 2019). Because our digital fracture models are mated fractures based on isotropic surfaces, future work should employ natural rock fractures with anisotropic characteristics (e.g., sheared fractures) to confirm the limitations of our proposed model.

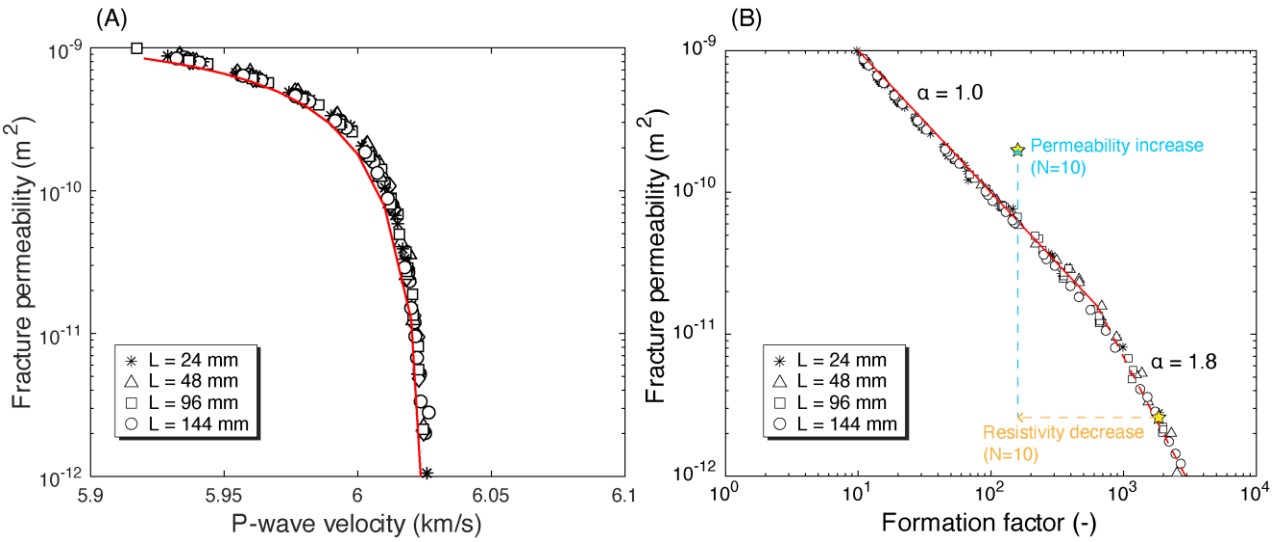

Figure 4: Graphs of fracture permeability versus (A) P-wave velocity and (B) formation factor. Symbol shapes represent different fracture sizes. *N* in Fig. 4 (B) indicates the number of fractures in a unit volume, and associated changes of permeability and resistivity are illustrated by blue and orange dashed arrows, respectively. Modified after Sawayama et al. (2020b).

3.3 Effect of water saturation on resistivity and elastic wave velocity

Changes in resistivity and elastic wave velocity with increasing water saturation were simultaneously measured through water-gas replacement tests. Figure 5 (A) shows observed resistivity at various ranges of frequency, and Figure 5 (B) shows observed elastic waveform. Plot colors in both figures change from red to blue following the saturation condition (from dry to brine saturated). The resistivity shows a significant decrease as water saturation increases and has almost no frequency dependence after brine injection (Fig. 5 (A)). Although resistivity could detect the saturation changes, the elastic waveform did not change even at the same condition as resistivity monitored.

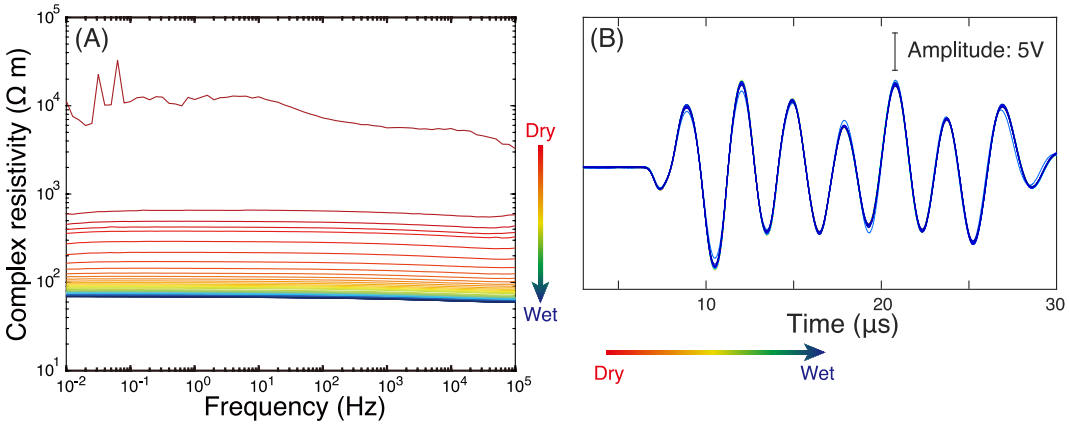

Figure 5: Experimental observation of continuous changes of resistivity and elastic waveform of GA-1 with brine injection into the dry fractured sample (data from Sawayama et al., 2018). (A) Complex resistivity measured in the direction parallel to the fracture at frequency ranges of 10 mHz to 100 kHz and (B) elastic waveform propagating to a direction perpendicular to the fracture.

Based on the experimental results, we further investigated the effect of water saturation on resistivity and elastic wave velocity at various aperture and saturation (assuming a random distribution of brine and nitrogen gas) conditions by finite-element and finite-difference methods. Figure 6 shows the log-log relationship between resistivity index (RI) and water saturation (S_w). Based on following Archie's law, the relationship must be linear:

$$\mathrm{RI} = \frac{\rho}{\rho_{sw=1}} = {S_w}^{-n},$$

where ρ and $\rho_{sw=1}$ denote the resistivity of rock and the resistivity at fully saturated conditions, respectively. And n is saturation exponent, which generally takes ~2 in sandstone (Guéguen and Palciauskas, 1994). As the results of experiment and finite-element simulation, experimental result and simulation result at 0.06 mm of aperture condition show a non-linear relationship between the logarithm of resistivity index and water saturation (i.e., a different value of n). Since n might be related to the connectivity of fluids (Guéguen and Palciauskas, 1994), this non-unique value of n indicates that connectivity of fluids is different at lower and higher saturation. In such conditions, Archie's law cannot be applicable as a unique value of n. Simulation results at 0.4 mm or larger aperture conditions show a unique value of n (~1.4 in this study) in all models, indicating that connectivity of fluids could be constant if the fracture aperture is large enough to realize connecting fluid flow. However, n tends to be varied at lower saturation condition (20% saturation) even at larger aperture condition. This might be due to the assumption of randomly distributed fluids. We further investigate whether it is realistic or not based on two-phase fluid flow LBM simulation (e.g., Shan-Chen model, Shan and Chen, 1993; Sawayama et al., 2020c).

Figure 7 (A) shows P-wave velocity variation versus water saturation at various aperture conditions. As the results of experiment and finite-difference simulations, experimental result and simulation result at 0.06 mm aperture condition show no saturation dependence, indicating that velocity in the direction perpendicular to such a small fracture could not detect saturation changes in the fractures. Simulation results at 0.4 mm or larger aperture conditions show the variation of velocity; however, the velocity changes are different from theoretical solutions based on Ray theory and effective medium theory in a parallel plane model (Mavko et al., 2009). This difference between our results and theoretical solutions may arise from the heterogeneity of fluid distribution; generally, a large contact area between fluids causes velocity reduction (e.g., Mavko et al., 2009). To evaluate this heterogeneity of fluid distribution, we calculated the contact area between fluids (Fig. 7 (B)). As a result, the contact area becomes bigger as the fracture aperture increases, and it has the largest value at ~50% saturation. Since we assumed a random distribution of fluids, 50% of saturation should have the largest value of contact area between fluids. Velocity change may depend not only on aperture or saturation, but also on fluid distribution; therefore, further study is needed to evaluate the realistic fluid distribution. The dependence of fluid distribution on both resistivity and velocity may cause difficulty for estimating water saturation from only resistivity or only velocity monitoring through traditional rock physical models. Our results suggest that integrated monitoring of resistivity and velocity might be useful to correct the dependence of fluid distribution on them, and hence contribute to evaluating water saturation precisely. The two-phase fluid flow simulation at various conditions such as wettability (Sawayama et al., 2020c) is needed for further discussion.

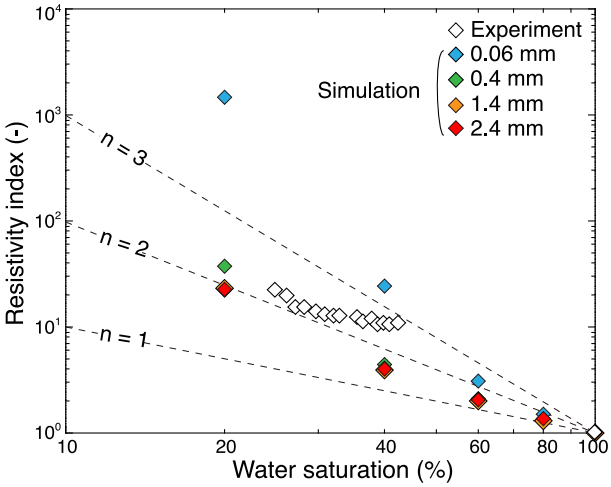

Figure 6: Experimental and simulation results of resistivity plotted as Archie's relation. Gray dashed lines indicate the ideal linear lines, which take 1, 2, 3 of saturation exponent *n*.

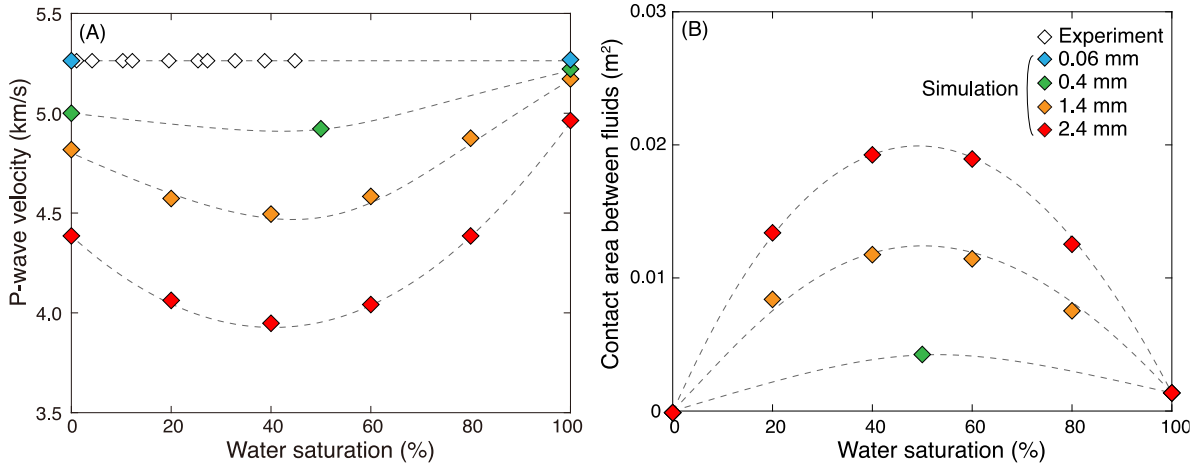

Figure 7: Variations of P-wave velocity and the contact area between fluids at various aperture conditions as a function of water saturation. (A) P-wave velocity and (B) contact area between fluids.

CONCLUSIONS

We investigated simultaneous changes in permeability, resistivity, and elastic wave velocity with aperture closure by coupling experiments and digital fracture simulation. Our results show that changes in permeability and resistivity are controlled by disconnection of flow paths, whereas velocity change is constrained by the roughness dependency of porosity. We further demonstrated that permeability could be empirically formulated as a function of velocity or resistivity regardless of fracture sizes, which indicates that laboratory-scale fracture properties can be confidently used for interpreting field data and for fracture flow monitoring by utilizing geophysical data.

We also discussed the effect of water saturation on resistivity and velocity at various aperture conditions. Although resistivity is influenced not only by water saturation but also by fluid distribution, Archie's law can be applicable as a unique n value (~1.4 at our research condition) at larger fracture aperture and higher saturation conditions. Velocity variation is affected by fracture aperture and water saturation as well as the contact area between fluids. Since both resistivity and velocity are influenced by fluid distribution, integrated monitoring of resistivity and velocity is needed to correct the effect of fluid distribution and thereby evaluate water saturation precisely.

ACKNOWLEDGEMENTS

The present study was supported in part by the Japan Society for the Promotion of Science (JSPS) through a Grant-in-Aid for JSPS Fellows (19J10125) and Grant-in-Aid for Young Scientists (18K14169 and 19K15100).

REFERENCES

Ahrenholz, B., Tölke, J., Lehmann, P., Peters, A., Kaestner, A., Krafczyk, M., and Durner, W.: Prediction of capillary hysteresis in a porous material using lattice-Boltzmann methods and comparison to experimental data and a morphological pore network model, Advances in Water Resources, 31, (2008), 1151–1173.

Andra, H., Combaret, N., Dvorkin, J., Glatt, E., Han, J., Kabel, M., Keehm, Y., Krzikalla, F., Lee, M., Madonna, C., and Marsh, M.: Digital rock physics benchmarks—Part II: Computing effective properties. Computers & Geosciences, 50, (2013), 33–43.

Archie, E, G.: The Electrical Resistivity Log as an Aid in Determining Some Reservoir Characteristics. Petroleum Technology, (1942), 54–62.

Bernabe, Y.: the Effective Pressure Law for Permeability in Chelmsford Granite and Barre Granite. International Journal of Rock Mechanics and Mining Sciences, 23, (1986), 267–275.

Bohlen, T., and Saenger, E. H.: Accuracy of heterogeneous staggered-grid finite-difference modeling of Rayleigh waves. Geophysics, 71, (2006), T109–T115.

Didana, Y.L., Heinson, G., Thiel, S., Krieger, L.: Magnetotelluric monitoring of permeability enhancement at enhanced geothermal system project. Geothermics, 66, (2017), 23–38.

Endres, A. L. and Knight, R.: The effects of pore-scale fluid distribution on the physical properties of partially saturated tight sandstones." Journal of Applied Physics, 69, (1991), 1091−1098.

Eng, C., Ikeda, T., and Tsuji, T.: Study of the Nankai seismogenic fault using dynamic wave propagation modelling of digital rock from the Nobeoka Fault. Exploration Geophysics, 49(1), (2018), 11–20.

Garboczi, E.J.: Finite element and finite difference programs for computing the linear electric and elastic properties of digital image of random materials., Natl. Inst.Stand.Technol.Interag.Rep.,6269, (1998).

Gassmann, F.: Uber die Elastizitat poroser Medien (Elasticity of porous media). Vierteljahrsschrift der Naturforschenden Gesselschaft in Zurich, 96, (1951), 1–23.

Guéguen, Y. and Palciauskas, V.: Introduction to the physics of rocks. Princeton, New Jersey, (1994), 294p.

He, X., and Luo, L. S.: Lattice Boltzmann model for the incompressible Navier–Stokes equation. Journal of statistical Physics, 88, (1997), 927–944.

Hermance, J.F.: The electrical conductivity of materials containing partial melt, a simple model from Archie's law. Geophysical Research Letters, 6, (1979), 613–616.

Ishibashi, T., N. Watanabe, N. Hirano, A. Okamoto, and N. Tsuchiya: Beyond-laboratory-scale prediction for channeling flows through subsurface rock fractures with heterogeneous aperture distributions revealed by laboratory evaluation, Journal of Geophysical Research: Solid Earth, 120, (2015), 106–124.

Jiang, F., Tsuji, T., and Hu, C.: Elucidating the Role of Interfacial Tension for Hydrological Properties of Two-Phase Flow in Natural Sandstone by an Improved Lattice Boltzmann Method. Transport in Porous Media, 104, (2014), 205–229.

Johnson, D.L.: Theory of frequency dependent acoustics in patchy-saturated porous media. Journal of Acoustic Society of America, 110, (2001), 682–694.

Kaieda, H.: Multiple Reservoir Creation and Evaluation in the Ogachi and Hijiori HDR Projects, Japan. Proceedings of the World Geothermal Congress 2015, (2015).

Kern, H.: The effect of high temperature and high confining pressure on compressional wave velocities in quartz-bearing and quartz-free igneous and metamorphic rocks, Tectonophysics, 44, (1978), 185–203.

Knight, R.: Hysteresis in the electrical resistivity of partially saturated sandstones. Geophysics, 56, (1991), 2139–2147.

Kirkby, A., Heinson, G., and Krieger, L.: Relating permeability and electrical resistivity in fractures using random resistor network models. Journal of Geophysical Research: Solid Earth, 121, (2016), 1546–1564.

Majer, E. L., Baria, R., Stark, M., Oates, S., Bommer, J., Smith, B. and Asanuma, H.: Induced seismicity associated with Enhanced Geothermal Systems. Geothermics, 36, (2007), 185–222.

Makarynska, D., Gurevich, B., Ciz, R., Arns, C. H., and Knackstedt, M. A.: Finite element modelling of the effective elastic properties of partially saturated rocks. Computers & Geosciences, 34, (2008), 647–657.

Mavko, G., Mukerji, T. and Dvorkin, J.: The Rock Physics Handbook Tools for Seismic Analysis of Porous Media. Cambridge University Press, Cambridge, (2009), 511p.

Murphy, W. F.: Effects of partial water saturation on attenuation in Massilon sandstone and Vycor porous glass. Journal of the Acoustical Society of America, 71, (1982), 1458–1468.

Nakatsuka, Y., Xue, Z., Garcia, H., and Matsuoka, T.: Experimental study on CO2 monitoring and quantification of stored CO2 in saline formations using resistivity measurements. International Journal of Greenhouse Gas Control, 4, (2010), 209–216.

Paterson, M. S. and Wong, T., 2004: Experimental Rock Deformation, The Brittle Field, 2nd ed. Springer-Verlag, New York, 347p.

Peacock, J. R., Thiel, S., Reid, P. and Heinson, G.: Magnetotelluric monitoring of a fluid injection: Example from an enhanced geothermal system." Geophysical Research Letters, 39, (2012), 3–7.

Peacock, J.R., Thiel, S., Heinson, G.S., Reid, P.: Time-lapse magnetotelluric monitoring of an enhanced geothermal system. GEOPHYSICS, 78, (2013), B121–B130.

Power, W. L., and Durham, W. B.: Topography of natural and artificial fractures in granitic rocks: Implications for studies of rock friction and fluid migration. International Journal of Rock Mechanics and Mining Sciences, 34, (1997), 979–989.

Power, W. L., Tullis, T. E., Brown, S. R., Boitnott, G. N., and Scholz, C. H.: Roughness of natural fault surfaces. Geophysical Research Letters, 14, (1987), 29–32.

Revil, A.: Effective conductivity and permittivity of unsaturated porous materials in the frequency range 1 mHz-1GHz. Water Resources Research, 49, (2013), 306–327.

Saenger, Erik, H., Gold, N., and Shapiro, Serge, A.: Modeling the propagation of elastic waves using a modified finite-difference grid. Wave Motion, 31, (2000), 77–92.

Sasada, M.: Inada granite, Chisitsu News, 441, 34–40, (1991), in Japanese.

Sandler, J., Li, Y., Horne, R. N., and Li, K.: Effects of fracture and frequency on resistivity in different rocks. In EUROPEC/EAGE Conference and Exhibition, Society of Petroleum Engineers, (2009).

Sawayama, K., Ishibashi, T., Jiang, F., Tsuji, T., and Fujimitsu, Y.: Relating Hydraulic-Electrical-Elastic Properties of Natural Rock Fractures at Elevated Stress and Associated Transient Changes of Fracture Flow. Earth and Space Science Open Archive, (2020a), 1–15.

Sawayama, K., Ishibashi, T., Jiang, F., Tsuji, T., Nishizawa O., and Fujimitsu, Y.: Scale-independent relationship between permeability and resistivity in mated fractures with natural rough surfaces. Earth and Space Science Open Archive, (2020b).

Sawayama, K., Jiang, F., Tsuji, T., and Fujimitsu, Y.: Development of two-phase fracture flow simulation method using Shan-Chen type lattice Boltzmann model. Proceedings of International Symposium on Earth Science and Technology, (2020c), 250–253.

Sawayama, K., Kitamura, K. and Fujimitsu, Y.: Laboratory measurements on electric and elastic properties of fractured geothermal reservoir rocks under simulated EGS conditions. GRC Transactions, 42, (2018a), 2459–2475.

Sawayama, K., Kitamura, K. and Fujimitsu, Y.: Relationship between Complex Resistivity, Elastic Wave and Water Saturation of Cracked Andesite under Laboratory Fluid-Flow Test. BUTSURI-TANSA (Exploration Geophysics), 71, (2018b), 71–85, in Japanese with English abstract.

Sawayama, K., Kitamura, K. and Fujimitsu, Y.: Effects of water saturation, fracture and salinity on electric and elastic properties of fractured geothermal rocks. Journal of the Geothermal Research Society of Japan, 41, (2019), 53–59.

Saxena, N., and Mavko, G.: Estimating elastic moduli of rocks from thin sections: Digital rock study of 3D properties from 2D images. Computers & geosciences, 88, (2016), 9–21.

Schmutz, M., A. Blondel, and A. Revil.: Saturation dependence of the quadrature conductivity of oil-bearing sands. Geophysical Research Letters, 39, (2012), 1–6.

Sen, P. N., and Goode, P. A.: Influence of temperature on electrical conductivity on shaly sands. Geophysics, 57(1), (1992), 89–96.

Shan, X., and Chen, H.: Lattice Boltzmann model for simulating flows with multiple phases and components. Physical review E, 47, (1993), 1815.

Su, Q., Feng, Q. and Shang, Z.: Electrical impedance variation with water saturation in rock. Geophysics, 65(1), (2000), 68–75.

Taira, T., Avinash, N., Brenguier, F., and Manga, M.: Monitoring reservoir response to earthquakes and fluid extraction, salton sea geothermal field, California. Science Advances, 4, (2018).

Tsuji, T., Ikeda, T., and Jiang, F.: Evolution of hydraulic and elastic properties of reservoir rocks due to mineral precipitation in CO2 geological storage. Computers & geosciences, 126, (2019), 84–95.

Watanabe, N., Hirano, N., and Tsuchiya, N.: Determination of aperture structure and fluid flow in a rock fracture by high-resolution numerical modeling on the basis of a flow-through experiment under confining pressure. Water Resources Research, 44, (2008), 1–11.

Witherspoon, P. A., Wang, J. S. Y., Iwai, K., and Gale, J. E.: Validity of Cubic Law for Fluid Flow in a Deformable Rock Fracture. Water Resources Research, 16, (1980), 1016–1024.

Yamabe, H., Tsuji, T., Liang, Y., and Matsuoka, T.: Influence of fluid displacement patterns on seismic velocity during supercritical CO2 injection: Simulation study for evaluation of the relationship between seismic velocity and CO2 saturation. International Journal of Greenhouse Gas Control, 46, (2016), 197–204.

Yamaya, Y., Takakura, S., Asanuma, H.: Resistivity monitoring of a geothermal reservoir at the Okuaizu geothermal field, Japan using the AMT method.” Journal of the Geothermal Research Society of Japan, 40, (2018), 159–173, in Japanese with English abstract.